Journal Pre-proof

Room temperature fabrication of oriented Zr-MOF membrane with superior gas selectivity with zirconium-oxo cluster source

Jiahui Yan, Taotao Ji, Yanwei Sun, Shengyan Meng, Chen Wang, Yi Liu

PII: S0376-7388(22)00704-9

DOI: https://doi.org/10.1016/j.memsci.2022.120959

Reference: MEMSCI 120959

To appear in: *Journal of Membrane Science*

Received Date: 2 June 2022

Revised Date: 10 August 2022

Accepted Date: 25 August 2022

Please cite this article as: J. Yan, T. Ji, Y. Sun, S. Meng, C. Wang, Y. Liu, Room temperature fabrication of oriented Zr-MOF membrane with superior gas selectivity with zirconium-oxo cluster source, *Journal of Membrane Science* (2022), doi: https://doi.org/10.1016/j.memsci.2022.120959.

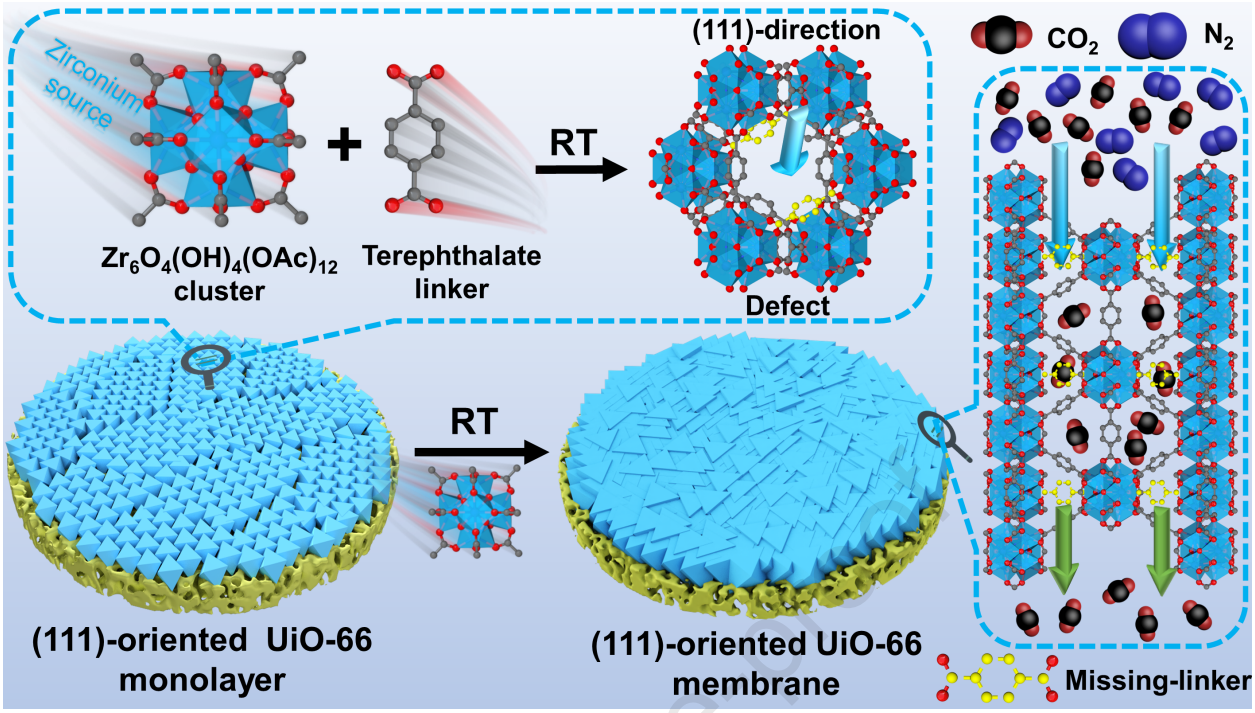

Room Temperature Fabrication of Oriented Zr-MOF Membrane with Superior Gas Selectivity with Zirconium-oxo Cluster Source

Jiahui Yan[a], Taotao Ji[a], Yanwei Sun[a], Shengyan Meng[a], Chen Wang[a] and Yi Liu[a,b]*

[a] State Key Laboratory of Fine Chemicals, School of Chemical Engineering, Dalian University of Technology, Linggong Road 2, Ganjingzi District, Dalian 116024, China

[b] Dalian Key Laboratory of Membrane Materials and Membrane Processes, Dalian University of Technology, Linggong Road 2, Ganjingzi District, Dalian, 116024, China

Abstract

Rational structural design and engineering of MOF membranes is particularly promising for energy-efficient gas separation. Preferred orientation manipulation delegates an effective approach to eliminate intercrystalline defects and therefore, improve their separation performance, while room-temperature (RT) synthetic protocol is quite beneficial to foster their industrial batch production. Nevertheless, it remains challenging to fabricate highly oriented MOF membranes at RT; simultaneously, the density of defective sites in the framework, which is assumed to exert significant influence on the separation performance relying on high affinity-interactions between guest molecules and coordinatively-unsaturated open metal sites, should be deliberately tailored. In this study, we achieve RT synthesis of highly (111)-oriented UiO-66 membrane exhibiting high defect density in the framework through employing $Zr_6O_4(OH)_4(OAc)_{12}$ clusters as zirconium source during epitaxial growth. Prepared UiO-66 membrane manifests an ideal CO_2/N_2 selectivity of 46.2, which represents the highest value among all pure MOF membranes tested in comparable operating conditions. It is anticipated that the above protocol can be further expanded for facile and mild preparation of state-of-the-art MOF membrane.

Keywords: Metal-organic framework; UiO-66; Defects; Orientation; Membrane

1. Introduction

Owing to the effective avoidance of energy-intensive thermally-driven phase changes, membrane process represents a promising option for energy-efficient gas separation compared with traditional separation processes like cryogenic distillation. The past decades witnessed significant progress made in metal-organic framework (MOF) membranes with superior prospect for applications in gas separation, benefiting from their tailorable pore aperture, ultrahigh porosity, framework flexibility, and rich functional groups [1-5]. It should be noted that, however, under most conditions MOF membrane growth has to be conducted at relatively high reaction temperature, which inevitably increases the capital investment, operating cost, and energy consumption for their batch production [6-10]. Moreover, owing to the thermal expansion coefficient discrepancy between MOF layers and substrates, substantial intergranular cracks may form during the heating/cooling process, thus leading to inferior gas separation performance [11,12]. Room temperature (RT) synthetic protocol offers a facile and reliable solution on the above concerns. Nevertheless, there remain few literatures on RT MOF membranes preparation apart from a minority of single-metal-based counterparts (e.g., HKUST-1 and ZIF-8 membranes) [12-14].

UiO-66, featuring $[Zr_6(\mu_3\text{-}O)_4(\mu_3\text{-}OH)_4]^{12+}$ node connected to terephthalic linkers with hexanuclear *fcu*-topology, represents a promising candidate of membrane materials because of its outstanding thermal/chemical stability, appropriate pore aperture, and rich functional groups [7,15-19]; in addition, high affinity-interactions between $Zr_6O_4(OH)_4$-node in defective frameworks and CO_2 render UiO-66 extremely appealing towards competent CO_2 separation [20-25]. Li et al. took the lead to prepare CO_2 permselective UiO-66 membranes at 120 °C via in situ growth [21]. Caro et al. fabricated UiO-66 membranes with H_2 permselectivity at 180 °C via secondary growth [26]. In a recent study, we fabricated highly CO_2 permselective UiO-66 membranes at 140 °C using tertiary growth with ZrS_2 source [22]. Very recently, Dong et al. synthesized ultra-thin UiO-66 membranes at 120 °C through in situ synthesis [7]. The difficulty in further reducing the temperature lies in that the pre-formation of

$Zr_6O_4(OH)_4$-node in bulk-solution, which delegates the rate-limited step, is required for further growth of continuous UiO-66 membrane [27,28].

Previous study revealed that structural defects in UiO-66 membranes at different scales cooperatively exerted significant influence on their CO_2/N_2 separation performance [20,29]. On the one hand, increasing density of framework defect (i.e., missing-linker number) at the microscopic scale was capable of boosting porosity (i.e., pore size, surface area and pore volume) and coordinately-unsaturated open metal-sites in UiO-66 frameworks, which was favorable for increasing both CO_2/N_2 selectivity and CO_2 permeability [20,28,30-35]. For instance, our recent study indicated that the UiO-66 membrane prepared with ZrS_2 source led to remarkably increased missing-linker numbers showing improved CO_2/N_2 selectivity, thereby demonstrating an obvious positive association between the CO_2/N_2 selectivity and missing-linker numbers [20,22]. Park et al. fabricated UiO-66-incorporated defect-tailored mixed-matrix-membranes exhibiting improved CO_2/N_2 separation performance so that the validity of defect-engineering on performance improvement for UiO-66-derived MMMs was verified [29]. On the other hand, preferred orientation control at the mesoscopic scale has been proven very efficacious in improving gas separation performance of MOF membrane, due to the reduction in grain boundary defects, ordered arrangement of micropore channel, and decrease in diffusion-path length for guest molecules [8,20,23,26,36-38]. Regarding UiO-66 membranes, previous literatures demonstrated that compared with randomly oriented or preferentially (002)-oriented counterparts, highly (111)-oriented UiO-66 membranes manifested both higher CO_2/N_2 selectivity and CO_2 permeance [20,39]. To ensure both the process simplicity and performance superiority, it is expected that highly (111)-oriented UiO-66 membranes exhibiting higher missing-linker numbers could be facilely prepared at RT.

Zirconium-oxo acetate cluster $Zr_6O_4(OH)_4(OAc)_{12}$ ($OAc=CH_3COO$), which is composed of metal-inorganic-oxides Zr-O-Zr core surrounded by acetate ligands, belongs to the tetravalent-transition-metallic-oxo clusters family and has been widely used well-defined building blocks for Zr-MOF

synthesis [27,28,40]. Benefiting from decent coordinative-interaction between acetate ligands and $Zr_6O_4(OH)_4$-core, employing $Zr_6O_4(OH)_4(OAc)_{12}$ clusters as zirconium source warrants lower activation-energy required for UiO-66 formation through pre-organization of $Zr_6O_4(OH)_4$-node in precursor solution as well as more accurate controlling of the missing-linker numbers through manipulating the ligand exchange rate [27]; simultaneously, conducting epitaxial growth under milder synthetic conditions is beneficial for suppressing twin generation and maintaining preferred orientations originated from UiO-66 seed monolayer [37], thus holding great promise for preparing highly (111)-oriented defect-engineered UiO-66 membranes showing unprecedented CO_2/N_2 separation performances at RT.

Through employing $Zr_6O_4(OH)_4(OAc)_{12}$ clusters as zirconium source, very recently we developed a RT protocol for synthesizing defect-rich UiO-66 membrane possessing superior CO_2/N_2 selectivity [41]. In this study, a multi-scale defect tailoring strategy is further proposed to prepare highly (111)-oriented defect-engineered UiO-66 membrane showing unprecedented CO_2/N_2 selectivity. The fabrication process is as follow (Fig. 1): Initially, $Zr_6O_4(OH)_4(OAc)_{12}$ clusters are manufactured according to a well-reported procedure [28]. Subsequently, using the above clusters source, uniform octahedral-shaped UiO-66 seeds are synthesized at RT. In the next step, highly (111)-oriented UiO-66 seed layer is prepared via dynamic air-liquid interfaces self-assembly (DALIAS) procedure. Finally, epitaxial growth is carried out with $Zr_6O_4(OH)_4(OAc)_{12}$ clusters source at RT, resulting in the ultimate formation of highly (111)-oriented defect-engineered UiO-66 membrane. Gas permeation results indicated that its ideal CO_2/N_2 selectivity (46.2) ranked the highest among all pure MOF membranes tested in comparable conditions.

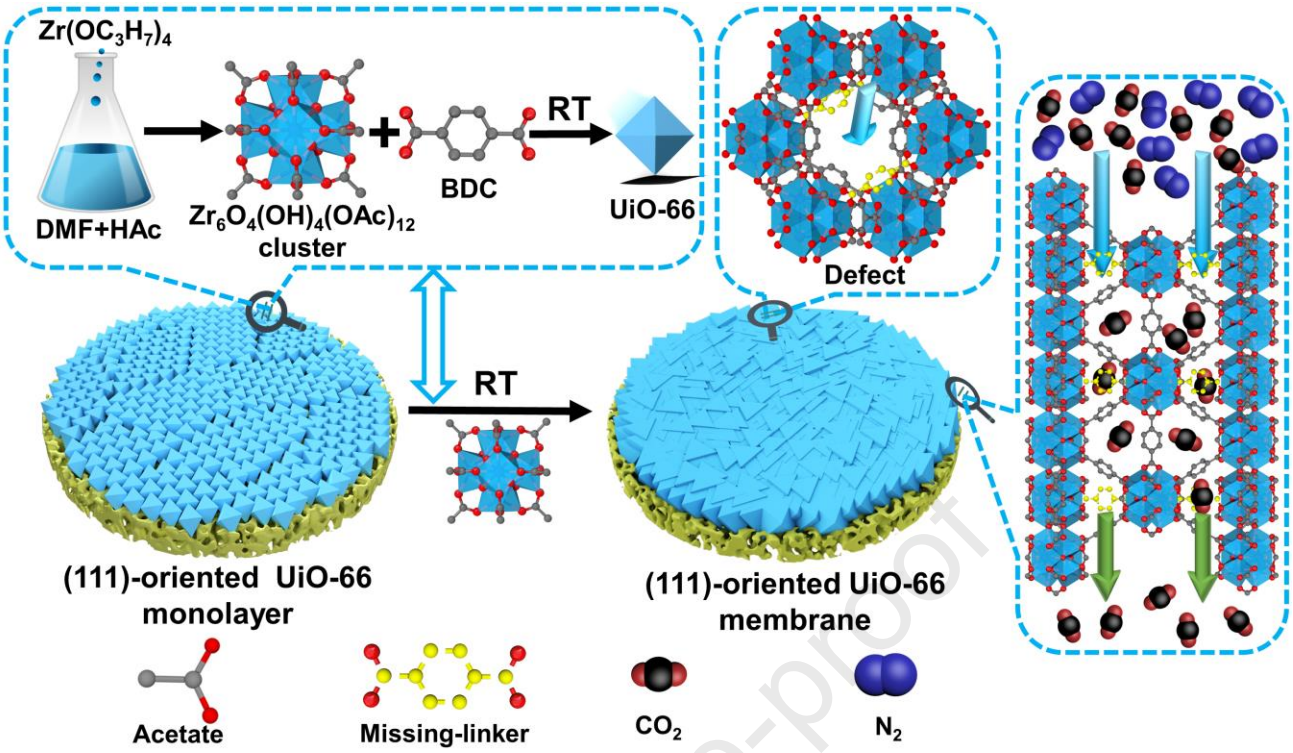

Fig. 1. Schematic representation of RT synthesis of highly (111)-oriented defect-engineered UiO-66 membrane employing $Zr_6O_4(OH)_4(OAc)_{12}$ clusters as zirconium source. Color codes: sky blue = $Zr_6O_4(OH)_4(OAc)_{12}$ clusters; grey = C; red = O.

2. Experimental section

2.1. Preparation of $Zr_6O_4(OH)_4(OAc)_{12}$ clusters

$Zr_6O_4(OH)_4(OAc)_{12}$ clusters were prepared according to the previous literature with slight modifications. Specifically, 0.31 g of $Zr(OC_3H_7)_4$ was added to binary HAc-DMF solvent (66 mL, V_{HAc}/V_{DMF}=24/42) followed by sonicating for 10 min. The clear solution was then transferred to a convective oven pre-heated to 130 °C, and kept for 3 h under this temperature. Ultimately, the vessel was taken out, allowed to cool naturally to RT. The cluster-containing solution color was changed from clear to yellow after the reaction (shown in SI-1).

2.2. Preparation of UiO-66 seeds

0.23 g of H_2BDC was added into 66 mL of the above cluster-containing solution, and then ultrasonicated for 20 min. Subsequently, this reaction was carried out for 6 h at RT. Acquired white

powders were separated through centrifugating, washing by ethanol and DMF six times, and ultimately drying for 12 h at 90 °C under vacuum.

2.3. Deposition of UiO-66 seed layers

2.3.1. Deposition of highly (111)-oriented UiO-66 seed layers

Initially, UiO-66 seeds (0.05 g) were uniformly dispersed in PVP aqueous solution (0.375 g/15 mL) followed by agitating for 24 h. Afterwards, UiO-66 seeds modified with PVP were centrifugated, rinsed with water six times, then dispersed in 4 mL of ethanol followed by sonication for 2 h. A regular-shaped container connected to the circulating-pump was filled with distilled-water prior to oriented deposition. In the next step, the above UiO-66 seed-containing suspension was spread on air/liquid interface employing the syringe injector until the final formation of a continuous seed layer. Through elevating the substrate to the air-liquid interface, the seed layer was automatically transferred to the substrate surface. Ultimately, the acquired seed monolayer was dried at 80 °C under vacuum for 12 h prior to use.

2.3.2. Deposition of randomly oriented UiO-66 seed layers

The seed suspension (0.3 wt.%) was fabricated through uniformly scattering UiO-66 seeds in ethanol followed by vigorous stirring for 3 days. Subsequently, the UiO-66 seed layers were uniformly deposited on surface of the substrates via spin-coating of 0.1 mL of seed suspension at 3,500 rpm for 1 min. Ultimately, the acquired seed layer was dried at 80 °C under vacuum for 12 h prior to use.

2.4. Epitaxial growth of UiO-66 membranes

2.4.1. Preparation of highly (111)-oriented UiO-66 membranes

Firstly, a Teflon-lined vessel (50 mL) was placed into an (111)-oriented UiO-66 seed monolayer-modified substrate vertically. Afterwards, the precursor solution obtained as the identical recipes and processing condition with UiO-66 seeds was poured into above vessel followed by conducting this reaction for 72 h at RT. Subsequently, the obtained UiO-66 membrane was taken out, washed by *n*-propanol, and ultimately dried under vacuum for 2 days at RT before gas permeation test.

Moreover, UiO-66 powders, which were deposited on the bottom of the vessels simultaneously after the reaction, were separated through centrifugating, washing by DMF and ethanol six times, and ultimately drying for 12 h at 90 °C under vacuum.

2.4.2. Preparation of randomly-oriented UiO-66 membranes

The detailed procedure for preparation of randomly-oriented UiO-66 membranes were the same to that of (111)-oriented UiO-66 membranes except that randomly-oriented UiO-66 seed layer-modified substrates were used instead.

2.5. Characterization

EDXS patterns and SEM images were obtained by Hitachi FlEXSEM-1000 instrument. The preferred-orientation, crystallinity and phase purity of prepared UiO-66 membranes and powders were investigated with Rigaku-SmartLab X-ray diffractometer using focused monochromatized Cu-Kα radiations at 200 mA and 45 kV. CO_2 (at 273 K and 298 K) and N_2 (at 77 K, 273 K and 298 K) adsorption isotherms on UiO-66 powders were assessed by the ASAP 2020 Plus (Micromeritics). Prior to measurement, the samples were dried and degassed for 900 min at 180 °C. The pore size distribution was calculated based on the Horvath-Kawazoe model by assuming a carbon-slit pore geometry determined by the software version 1.03 provided by Micromeritics. Functional groups in UiO-66 powders were characterized using FT-IR (Thermo Nicolet IS50) with KBr wafer. ATR-IR spectra were tested on Thermo Fisher iN10. TG analysis were measured on TG 209 (NETZSCH) under air purge in a temperature range between 40 °C and 900 °C with the ramping rate of 5 $°C \cdot min^{-1}$. DSC curves were recorded on DSC 204 F1 (NETZSCH) with aluminum crucible under air purge in a temperature range between 40 °C and 580 °C with the ramping rate of 5 $°C \cdot min^{-1}$. Prior to TG and DSC measurements, samples were activated for 720 min at 150 °C. The liquid ^1H NMR spectra were measured using the nuclear-magnetic-resonance spectrometer (Varian DLG400).

2.6. Gas permeation test

Both mixed-gas and single-gas permeation properties were tested with Wicke-Kallenbach technique. Obtained UiO-66 membranes were placed and sealed in membrane modules. The volume flow rates in feed side (single-gas or binary gas-mixture) were set to 50 mL·min^{-1}, and Helium was employed to sweep permeate side at a same flow rate. Pressure differences in the both sides was maintained at 0.1 MPa. In the separation test with humid feed gas, the feed gas was saturated with water vapor by flowing through a pure water tank (kept constantly at 60 °C) before entering the membrane permeation cell. Molar concentrations of permeated gases were analyzed with the calibrated gas-chromatograph (Agilent 7890B). Gas permeance ($\boldsymbol{P_i}$) was represented as a molar flow rate ($\boldsymbol{J_i}$) divided by permeate area ($\boldsymbol{A}$) and partial pressure difference ($\Delta\boldsymbol{P_i}$) (i.e., driving force) of component $\boldsymbol{i}$:

$$\boldsymbol{P_i}(\textbf{permeance}) = \frac{\boldsymbol{J_i}}{\Delta\boldsymbol{P_i}\ x\ \boldsymbol{A}}$$

The ideal selectivity ($\boldsymbol{\alpha_{A/B}}$ (**ideal**)) was calculated by the single-gas permeance ratios for gas pair A/B:

$$\boldsymbol{\alpha_{A/B}}(\textbf{ideal}) = \frac{\boldsymbol{P_A}(\textbf{permeance})}{\boldsymbol{P_B}(\textbf{permeance})}$$

Separation factor ($\boldsymbol{\alpha_{A/B}}$) was expressed to the quotients of molar fraction of component A/B on both sides:

$$\boldsymbol{\alpha_{A/B}} = \frac{\boldsymbol{X_{A,perm}}/\boldsymbol{X_{B,perm}}}{\boldsymbol{X_{A,feed}}/\boldsymbol{X_{B,feed}}}$$

Gas permeability ($\boldsymbol{P_i}$) was determined through multiplying the gas permeance by the effective thickness of the MOF membranes ($\boldsymbol{L}$):

$$\boldsymbol{P_i}(\textbf{permeability}) = \boldsymbol{P_i}(\textbf{permeance}) \times \boldsymbol{L}$$

$\boldsymbol{P_i}$ **(permeability)** was commonly expressed in Barrer (1 Barrer = 10^{-10} cm^3 (STP) ·cm^{-1}·s^{-1}·cmHg^{-1}).

3. Results and discussion

3.1. Preparation of defect-engineered UiO-66 seeds

Initially, $Zr_6O_4(OH)_4(OAc)_{12}$ clusters, which served as zirconium source, were synthesized under solvothermal conditions starting from zirconium propoxide solution (SI-1) [28,41]. Uniformly octahedral-shaped UiO-66 crystals with the grain sizes in the range of 300 nm to 2 μm could be faciely synthesized employing the above $Zr_6O_4(OH)_4(OAc)_{12}$ clusters source at RT (SI-2). It was found that the crystal size could be easily and precisely regulated by altering the synthesis time. Subsequently, 450 nm-sized UiO-66 crystals were chosen as seeds through balancing substrate surface roughness and seed layer thickness (Fig. 2a). Relevant FT-IR spectrum of above UiO-66 seeds exhibited characteristic bands at 1393 cm^{-1} (C=O symmetric stretching-vibration), 1506 cm^{-1} (C=C stretching-vibration), 1582 cm^{-1} (C=O antisymmetric stretching-vibration), and 1652 cm^{-1} (C=O stretching-vibration), which corresponded to carboxylate groups located in both BDC linkers and acetate (SI-3) [7,42].

TG-DSC analysis was then carried out to quantify the deficiencies of BDC linkers in the UiO-66 framework. As shown in Fig. 2b, both weight losses of TGA traces and exothermic peaks of DSC traces in the range of 40-200 °C, 200-310 °C, 310-390 °C, and 390-515 °C, which corresponded to de-solvation (H_2O and DMF), de-hydroxylation, modulator removal (acetic acid), and framework decomposition, respectively, matched well with previous reports [43]. Correspondingly, missing-linker numbers per $Zr_6O_4(OH)_4$-node in the framework of UiO-66 seeds was calculated to be 1.69 according to a procedure established via Lillerud et al. (detailed calculation procedures were shown in SI-4) [33]. Furthermore, textural properties of activated UiO-66 seeds were investigated through N_2 adsorption-desorption tests. The representative type-I isotherm with a sharp increase in N_2 uptakes in low relative pressures region revealed the microporous nature of UiO-66 seeds (Fig. 2c). Their BET surface area and micropore volume were calculated as 1331.2 $m^2 \cdot g^{-1}$ and 0.56 $cm^3 \cdot g^{-1}$, respectively, which were comparable with those of UiO-66 powders synthesized with other zirconium sources [28,30,31,33,43]. Simultaneously, the micro-pore size distributions caculated by the Horvath-Kawazoe-method implied that the average pore size of UiO-66 seeds was 0.66 nm (Fig. 2c).

3.2. Preparation of (111)-oriented UiO-66 membranes

Initially, a facile DALIAS method developed in our group was adopted to deposit UiO-66 seeds onto oriented seed layer. As shown in Fig. 2d-e, a uniform close-packed UiO-66 monolayer with a thickness of 450 nm was obtained (SI-5). Corresponding XRD pattern further confirmed the dominance of (111)-preferred orientation of the seed monolayer (Fig. 2i). Moreover, we observed that UiO-66 seed layer could be sub-divided into some isolated regions where octahedron-shaped UiO-66 crystals arranged themselves to hexagonal array, i.e., in-plane orientation (SI-6). As confirmed by our recent study, maintaining both regional in-plane and out-of-plane orientations could be advantageous for decreasing anisotropic grain boundaries and therefore, improving gas separation performance of UiO-66 membranes [23].

Subsequently, RT epitaxial growth was conducted to eliminate grain boundary gaps in the seed monolayer with $Zr_6O_4(OH)_4(OAc)_{12}$ clusters as zirconium source. SEM results showed that after epitaxial growth, a twin-free and well-intergrown UiO-66 membrane (abbreviated as ORI-UiO-M25) with smooth surface morphology had been formed (Fig. 2f). Corresponding EDXS results showed a distinct boundary between Zr and Al elements, thus demonstrating that obtained membranes did not infiltrate deep in the α-Al_2O_3 pore, which was favourable to decrease the diffusion path length of guest molecules (Fig. 2h). Cross-sectional SEM image revealed that thickness of ORI-UiO-M25 reached ~800 nm (Fig. 2g), which was thinner than majority of UiO-66 membranes synthesized at higher temperature [10,20-24,26]. Moreover, both out-of-plane and in-plane orientations derived from the seed monolayer were well preserved after epitaxial growth, which was beneficial for further decreasing crystallographic misorientations and grain boundary defects of the UiO-66 membranes (SI-6) [23]. In addition, relevant XRD pattern displayed mere diffraction peaks originated from (111), (222) and (333) crystal plane (Fig. 2i), thus further verifying the dominance of (111)-preferred orientation.

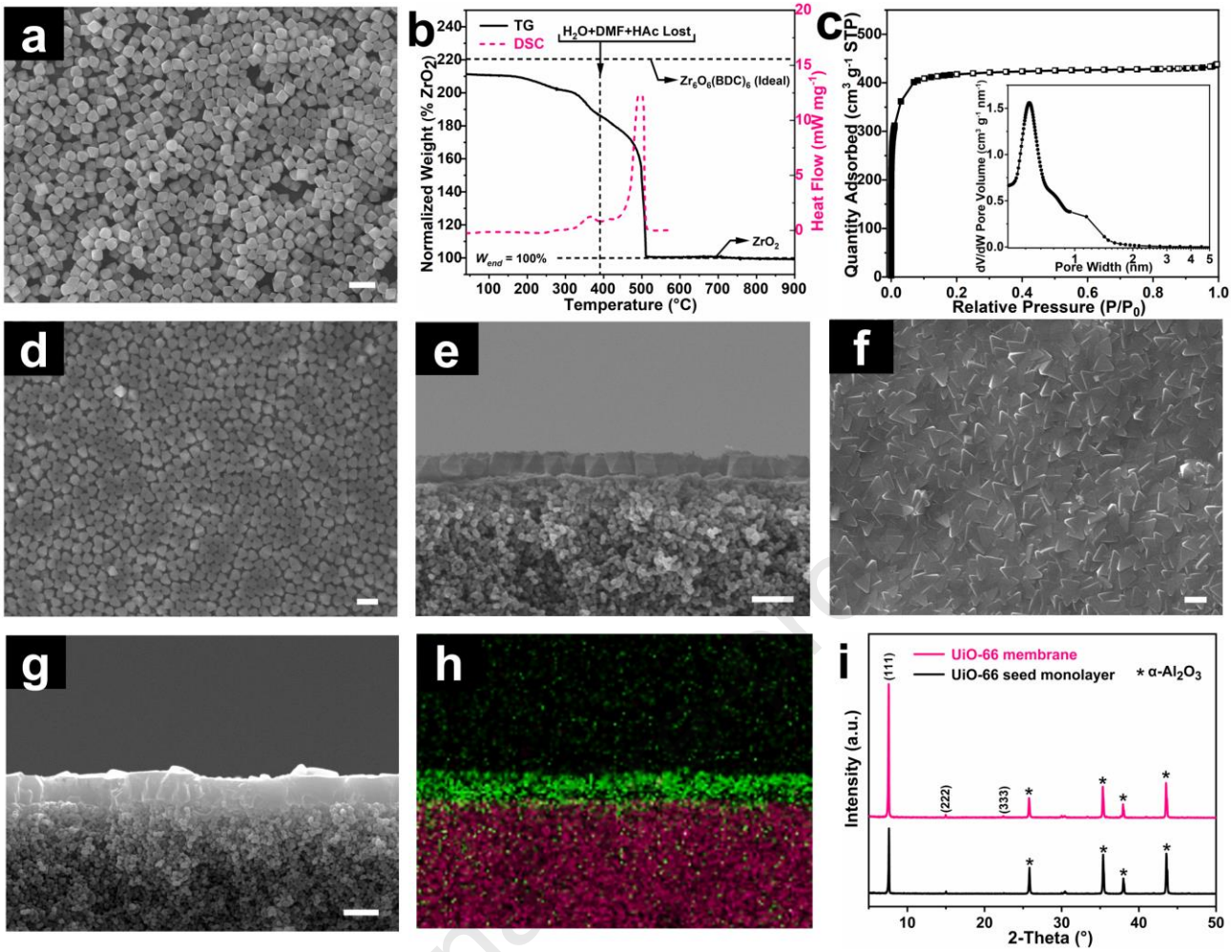

Fig. 2. (a) SEM image, (b) TG-DSC curve and (c) adsorption-desorption-isotherm of N_2 at 77 K (inset: HK-method-derived micropore size distribution) of UiO-66 seeds. (d) Top and (e) cross-sectional SEM images of UiO-66 seed monolayer. (f) Top and (g) cross-sectional SEM images of ORI-UiO-M25. (h) Cross-sectional EDXS image of ORI-UiO-M25 (color codes: Zr signals = green; Al signals = pink). (i) Corresponding XRD patterns. Scale bar: 1 μm.

Considering the significant influence of reaction temperature on membrane microstructure, epitaxial growth was further carried out on UiO-66 seed layers using $Zr_6O_4(OH)_4(OAc)_{12}$ cluster source at 90 °C (abbreviated as ORI-UiO-M90), 110 °C and 140 °C, respectively. It was found that increasing the reaction temperature inevitably resulted in the generation of substantial twin crystals; moreover, both twin density and grain size increased with increasing reaction temperature (Fig. 3a-i). To further quantify the degree of preferred orientation of the above UiO-66 membranes, their crystallographic

preferred orientation (CPO) indices were determined (details were shown in SI-7) [26,44,45]. Indices of CPO of the (111) reflection in relation to the (002) reflection (denoted as $CPO_{111/002}$) of UiO-66 membranes synthesized at 90 °C, 110 °C and 140 °C were calculated as 52.3, 35.4 and 6.3, respectively (SI-7). In contrast, no (002) reflection in the XRD pattern could be discriminated for ORI-UiO-M25 (Fig. 2i). It had been proven that random attachment of MOF nuclei formed in the bulk solution to the seed layer was the main cause of crystal twinning during epitaxial growth [37]. To elucidate this issue, the powder yield (PY), which could be used as an indicator of the degree of UiO-66 nucleation in bulk solution, was calculated according to molar contents of zirconium in precursor solution. Our results indicated that PY remarkably increased from 39.6% (25 °C) to 78.4% (140 °C) with increasing reaction temperature (SI-8), implying that the degree of UiO-66 nucleation in bulk solution was positively correlated with the reaction temperature. We therefore concluded that conducting the reaction at lower temperature was beneficial for preserving the preferred-orientations inherited from UiO-66 seed monolayer, owing to more effective inhibition of UiO-66 nucleation in bulk solution under such conditions.

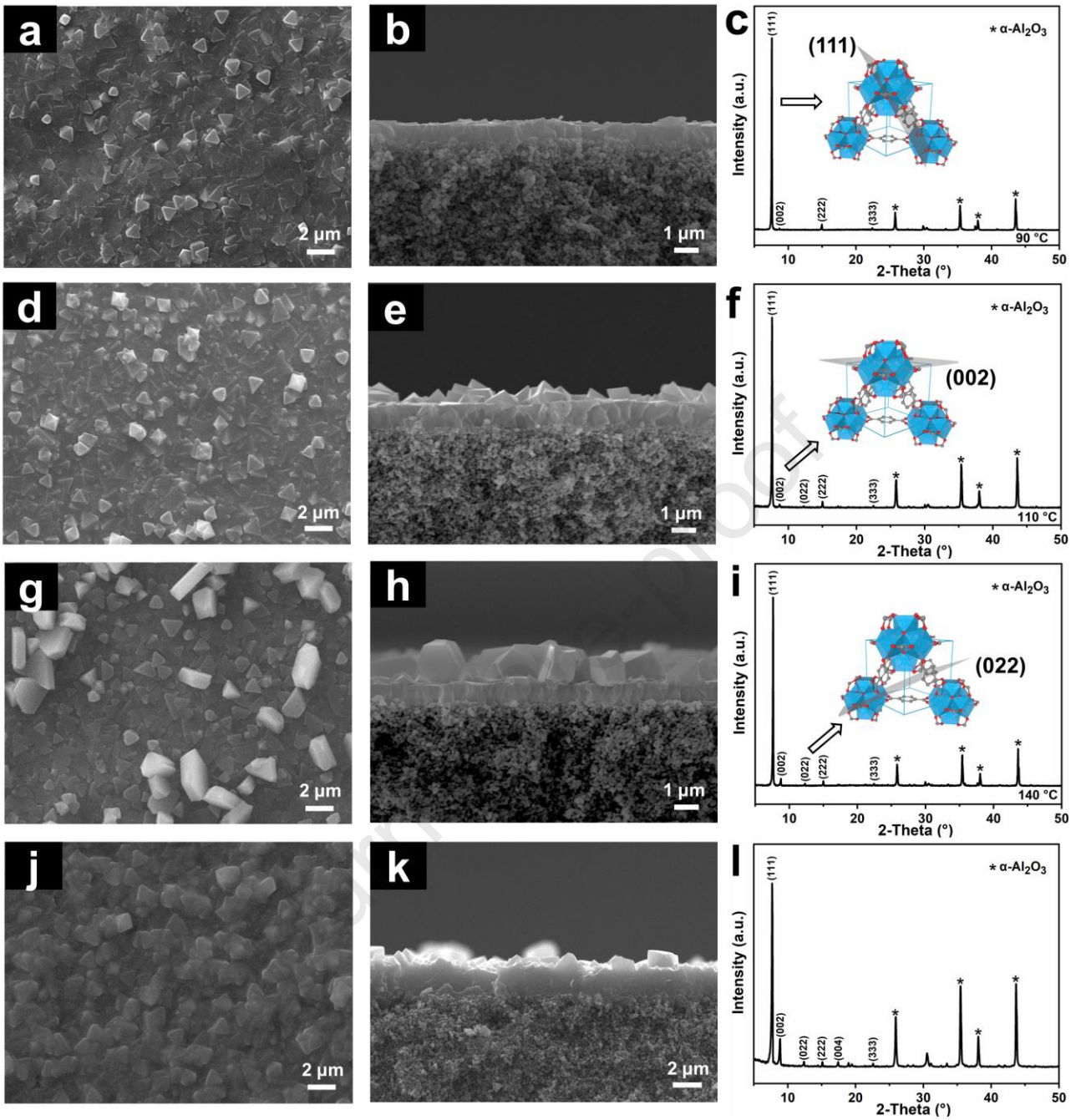

Fig. 3. SEM images and XRD patterns of (111)-oriented UiO-66 membranes prepared at (a-c) 90 °C, (d-f) 110 °C and (g-i) 140 °C. (j-l) SEM images and XRD pattern of randomly oriented UiO-66 membrane prepared at 25 °C.

3.3. Investigation of textural properties of the UiO-66 membrane

To elucidate more thoroughly the interplay between membrane structure and separation performance,

besides ORI-UiO-M25 and ORI-UiO-M90, simultaneously, UiO-66 powders deposited on bottom of the vessels (abbreviated as UiO-P25 and UiO-P90, respectively) were collected and studied further. As shown in Fig. 4a and 4e, XRD patterns and FT-IR spectra of UiO-P25 and UiO-P90 were in agreement to the typical UiO-66 phase, thereby confirming that the change in reaction temperature had no effect on their phase purity.

Furthermore, TG-DSC analysis was carried out to evaluate the missing-linker numbers in above UiO-66 samples (Fig. 4b). Experimental results indicated that the numbers of missing-linkers per $Zr_6O_4(OH)_4$-node in defective framework of UiO-P25 and UiO-P90 were 1.60 and 0.84, respectively, thus indicating that reducing the reaction temperature would give rise to higher missing-linker number. This is because the binding strength between capping groups and $Zr_6O_4(OH)_4$ nodes at RT is so high that it is more difficult to exchange the above capping reagents with BDC linkers at RT [28]. Moreover, compared with UiO-P90, conspicuous diffraction reflection of UiO-P25 in the 2θ range of 2-6° could be observed (Fig. 4c), implying the existence of a supernumerary defective-reo-phase, i.e., missing-nodes defects, in the UiO-66 framework [29,34]. It is worth mentioning that in such defective-reo-phase, per $Zr_6O_4(OH)_4$ node has lower linker connectivity compared with a perfect framework, thus jointly contributing to higher framework defect densities [31].

Possible terminal groups in defective UiO-66 framework were commonly hydroxy groups, chloride and monocarboxylates (i.e., deprotonated modulators such as acetate) [7,33]. The liquid ^{1}H NMR spectra recorded on fully activated UiO-P25 and UiO-P90 exhibited only three signals in the full chemical shift range (SI-9), which could be assigned to acetate, BDC and NMR solvent (Fig. 4d). This evidently confirmed that acetate indeed compensated for positively charged defects in the UiO-66 framework. Moreover, the acetate/BDC molar ratio of UiO-P25, as could be determined by the integral area of ^{1}H NMR, was higher than UiO-P90, implying that the concentration of acetate for terminating defects in the UiO-66 framework increased with increasing missing-linker numbers there [7,33]. While chloride could be ruled out due to the absence of chlorine elements in EDXS spectra of UiO-P25 and

UiO-P90 (SI-10). FT-IR spectra of hydroxyl groups on fully activated UiO-25 and UiO-P90 exhibited characteristic bands at 3644 and 3676 cm^{-1}, corresponding to μ_3-OH stretching in $[Zr_6(\mu_3\text{-}O)_4(\mu_3\text{-}OH)_4]^{12+}$-nodes (Fig. 4e) [46]. An additional OH adsorption band at 3691 cm^{-1} demonstrated that missing-linker sites were partially occupied by nonhydrogen-bonded OH group [47]. In view of the above results, we confirmed that defective sites in the framework of UiO-66 were jointly terminated by acetate and nonhydrogen-bonded OH group (Fig. 4k); moreover, IR band intensity of nonhydrogen-bonded OH group in UiO-P25 was higher than UiO-P90, thus demonstrating that higher content of nonhydrogen-bonded OH group existed on $[Zr_6(\mu_3\text{-}O)_4(\mu_3\text{-}OH)_4]^{12+}$-nodes as increasing missing-linker number [46].

To gain more insights into the impact of missing-linker number on their adsorption properties, N_2 adsorption-desorption-isotherms of UiO-P25 and UiO-P90 were measured at 77 K. As shown in Fig. 4f, BET surface areas of UiO-P25 and UiO-P90 were calculated as 1299.7 and 1032.7 $m^2 \cdot g^{-1}$, respectively, which were positively correlated with the missing-linker numbers. The increase in missing-linker numbers in the frameworks in turn contributed to enlarged pore size and increased accessible pore volumes [28,29]. Indeed, both the average pore size and micropore volume of UiO-P25 (0.65 nm and 0.52 $cm^3 \cdot g^{-1}$) were remarkably higher than UiO-P90 (0.6 nm and 0.46 $cm^3 \cdot g^{-1}$) (Fig. 4g and SI-11). In addition, adsorption-isotherms of CO_2 and N_2 on the UiO-66 powders were measured at 25 °C and up to 1 bar (Fig. 4h). It was observed that CO_2 adsorption capacities of UiO-P25 and UiO-P90 achieved 50.3 and 43.1 $cm^3 \cdot g^{-1}$ STP at 1 bar, respectively, thus verifying the validity of defect-engineering in enhancing CO_2 absorption properties; in contrast, their disrepancies in N_2 adsorption capacities were negligible. This phenomenon could be reasonably attributed to preferential CO_2 adsorption on more coordinatively-unsaturated open metal-sites in more defective UiO-66 frameworks [20,22,41].

Subsequently, isosteric adsorption heat (Q_{st}) of CO_2 on UiO-P25 and UiO-P90 were calculated from temperature-dependent isotherms at 273 and 298 K using the Clausius-Clapeyron equation (SI-12).

Fig. 4i showed that Q_{st} of CO_2 on UiO-P25 was higher than UiO-P90 in the whole range of adsorbed CO_2 loadings, implying that Q_{st} of CO_2 was positively correlated with the missing-linker numbers in UiO-66 frameworks due to stronger affinity-interactions between more defective $Zr_6O_4(OH)_4$ node and CO_2 [25,48]. This was in accordance with a previous study showing that the binding energy for CO_2 to defective $Zr_6O_4(OH)_4$-nodes capped with OH groups (-36 kJ·mol^{-1}) was higher than those of perfect $Zr_6O_4(OH)_4$-nodes (-30.32 kJ·mol^{-1}) [49]. In addition, Q_{st} of CO_2 on UiO-P25 increased with increasing adsorbed CO_2 loadings, possibly owing to strengthened adsorbate-adsorbate intermolecular interactions in the restricted pore space [48].

Based on the IAST method, the adsorption selectivity of CO_2/N_2 on UiO-P25 (CO_2/N_2=50:50) was calculated to 25.1 (at 25 °C and 1 bar) (SI-13), which was superior to that of UiO-P90 (21.5) (Fig. 4j). Since selectivity of the membrane ($S_{mem(i/j)}$) could be expressed as the product of diffusion-selectivity ($S_{diff(i/j)}$) and adsorption-selectivity ($S_{ads(i/j)}$) through the formula of $S_{mem(i/j)} = S_{diff(i/j)} \times S_{ads(i/j)}$ [50], possessing higher CO_2/N_2 adsorption selectivity would result in higher membrane selectivity toward the gas pair of CO_2/N_2; in addition, enlarging the pore size was beneficial for enhancing the gas permeance of CO_2 molecules through the membrane [7]. Therefore, possessing higher missing-linker numbers in the UiO-66 frameworks was anticipated to enhance separation performances of UiO-66 membranes towards the CO_2/N_2 gas pair.

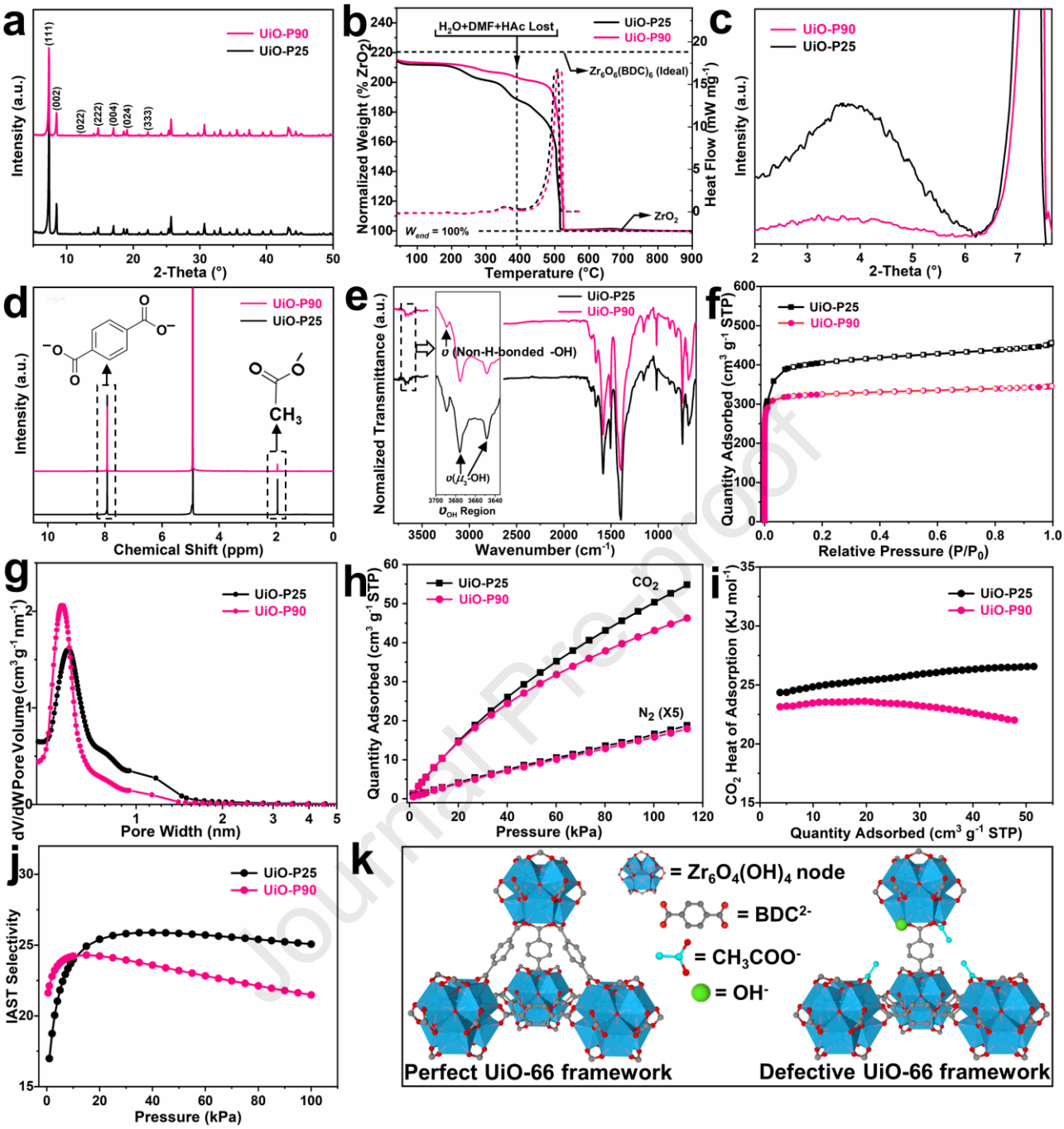

Fig. 4. (a) XRD patterns, (b) TG-DSC curves, (c) XRD patterns at low-2θ region, (d) Liquid ^{1}H NMR spectra, (e) FT-IR spectra (inset: υ_{OH} region), (f) adsorption-desorption-isotherms of N_2 (77 K), (g) pore size distribution, (h) adsorption isotherms of CO_2 and N_2 (298 K), (i) Q_{st} of CO_2, and (j) CO_2/N_2 IAST selectivity of UiO-P25 and UiO-P90. (k) Illustration depicting the compositional and structural differences between the defect-free UiO-66 and those with missing-linker defects.

As discussed above, carrying out epitaxial growth at RT through employing $Zr_6O_4(OH)_4(OAc)_{12}$ clusters as zirconium source warranted not only higher missing-linker numbers in UiO-66 frameworks at the microscopic scale but also better maintance of preferred orientation inherited from UiO-66 seed monolayer at the mesoscopic scale. We therefore deduced that CO_2/N_2 separation performance of ORI-UiO-M25 could be significantly enhanced compared with its randomly oriented and/or lower missing-linker numbered counterparts.

3.4. Evaluation of gas separation performances of UiO-66 membranes

To evaluate gas permeation properties on ORI-UiO-M25 under ambient conditions, volumetric flow rate of single-gas and binary gas-mixture through the membrane was determined. As shown in Fig. 5a, we found that there was no direct relationship between gas permeance and kinetic diameters of gas molecules due to a relatively large aperture size of UiO-66. Therefore, the gas permeation behaviors were dominated by preferential adsorption [20-22,24,41]. As expected, ORI-UiO-M25 exhibited the highest permeance towards CO_2 molecules (5.7×10^{-8} $mol\cdot m^{-2}\cdot s^{-1}\cdot Pa^{-1}$), due to the strong affinity-interactions between coordinatively-unsaturated open metal-sites in $Zr_6O_4(OH)_4$ node and CO_2 molecules (SI-14). Moreover, the highest ideal CO_2/N_2 selectivity of ORI-UiO-M25 achieved 46.2, which had far exceeded corresponding Knudsen diffusion coefficients (Fig. 5a). It should be addressed that ideal CO_2/N_2 selectivity of ORI-UiO-M25 ranked the highest among all pure MOF membranes tested in comparable conditions (Fig. 5d), thus confirming that multi-scale defect tailoring represented an appealing protocol to exceed performance limits of state-of-the-art MOF membranes (SI-15). In addition, compared with the results of single-gas permeations, CO_2 permeance in gas mixture was slightly decreased (Fig. 5a), which could be interpreted by the competitive adsorption between CO_2 and N_2 molecules in UiO-66 frameworks [8,24].

To verify the influence of preferred orientation on CO_2/N_2 separation performance, randomly oriented UiO-66 membrane (abbreviated as RAN-UiO-M25) was also prepared (SI-16). SEM images

revealed that RAN-UiO-M25 was well-intergrown with a thickness of 2.4 μm (Fig. 3j-k). Gas permeation results showed that RAN-UiO-M25 exhibited an ideal CO_2/N_2 selectivity of 24.9 with a CO_2 permeance of 2.1×10^{-8} $mol\cdot m^{-2}\cdot s^{-1}\cdot Pa^{-1}$ (Fig. 5b and SI-14). Compared with ORI-UiO-M25, both the CO_2 permeance and CO_2/N_2 selectivity of RAN-UiO-M25 were remarkably reduced, which could be attributed to the increased membrane thickness and grain boundary defects, respectively. Therefore, preferred orientation control indeed played decisive roles in enhancing the CO_2/N_2 separation performances of UiO-66 membranes.

Moreover, gas permeation behaviors on ORI-UiO-M90 were measured to confirm the effect of missing-linker number on the CO_2/N_2 separation performance. Our results indicated that in comparison with ORI-UiO-M25, ORI-UiO-M90 displayed decreased ideal CO_2/N_2 selectivity of 32.3 (Fig. 5c). This could be attributed to the lower number of missing-linkers in framework of ORI-UiO-M90, resulting in lower CO_2/N_2 adsorption selectivity. In addition, we noticed that the CO_2 permeability of ORI-UiO-M25 was close to that of ORI-UiO-M90, which could be interpreted as follow: Gas permeability equaled the product of diffusion-coefficient (*D*) and absorption-coefficient (*S*). *S* was equated to the absorbed concentration of guest molecules in upstream sides divided by the corresponding partial pressures in the membranes, while *D* was positively associated with jump length and random walk-jumping frequency of guest molecule [51]. In this study, ORI-UiO-M90 possessing lower missing-linker number manifested lower CO_2 absorption capacity, thus leading to decreased *S*; while owing to the weaker affinity-interactions between $Zr_6O_4(OH)_4$-node in the framework of ORI-UiO-M90 and CO_2 as confirmed by the lower Q_{st} of CO_2 (Fig. 4i), the motion or desorption of CO_2 molecules were promoted, i.e., jump length and random walk jumping frequency were increased, thereby giving rise to increased *D*. The counteracting effect between *S* and *D* ultimately contributed to similar CO_2 permeability [10,41]. Therefore, tailoring missing-linker defects could be a powerful tool for enhancing the CO_2/N_2 separation performances of UiO-66 membranes.

In addition, we further investigated separation performance towards CO_2/N_2 on ORI-UiO-M25

through imitating the composition (V_{CO2}:V_{N2}=15:85) of flue gases. The membrane kept CO_2/N_2 separation factor (SF) of 32.9 without reduction on CO_2 permeance (Fig. 5e); in effect, CO_2/N_2 SF of ORI-UiO-M25 was steadily kept above 30 in the full range of feed composition. In addition, no discernible decrease of CO_2/N_2 SF and CO_2 permeance could be discerned during the long-term test under ambient conditions (Fig. 5f), thereby holding great promise for the application under practical operating conditions. Finally, the adhesion strength of ORI-UiO-M25 was studied. Our research showed that even after ultrasonication for 60 min in DI water (shown in SI-17), ORI-UiO-M25 remained intact in morphology and steadily adhered to the substrate surface, thus demonstrating its excellent mechanical stability.

In addition, the influence of water vapor (~3.9 wt.%) on CO_2/N_2 separation performance of ORI-UiO-M25 was further investigated. After the introduction of saturated water vapor, ORI-UiO-M25 exhibited CO_2/N_2 separation factor (SF) of 33.7 with the CO_2 permeance of 4.4×10^{-8} $mol\cdot m^{-2}\cdot s^{-1}\cdot Pa^{-1}$, corresponding to 14% reduction in CO_2/N_2 SF and 26.2% reduction in CO_2 permeance. The long-term stability test in the presence of humid feed gas indicated that ORI-UiO-M25 exhibited stable CO_2/N_2 separation performance within 7 h. Further prolonging the duration led to an immediate deterioration in CO_2/N_2 SF, which could be attributed to the presence of more missing-linker defects in the UiO-66 framework.

ORI-UiO-M25 was further subjected to CO_2/N_2 separation at elevated operating temperature. It was found that operating temperature strongly affected the CO_2 permeance and CO_2/N_2 SF of ORI-UiO-M25. With increasing operating temperature from 25 to 120 °C, the CO_2 permeance steadily increased, whereas the CO_2/N_2 SF was remarkably reduced, which could be attributed to weakened affinity-interactions between coordinatively-unsaturated open metal-sites in defective $Zr_6O_4(OH)_4$ nodes and CO_2 at higher temperature [8]. In addition, ORI-UiO-M25 displayed inferior operation stability at 120 °C, which could be attributed to the presence of more missing-linker defects in the UiO-66 framework.

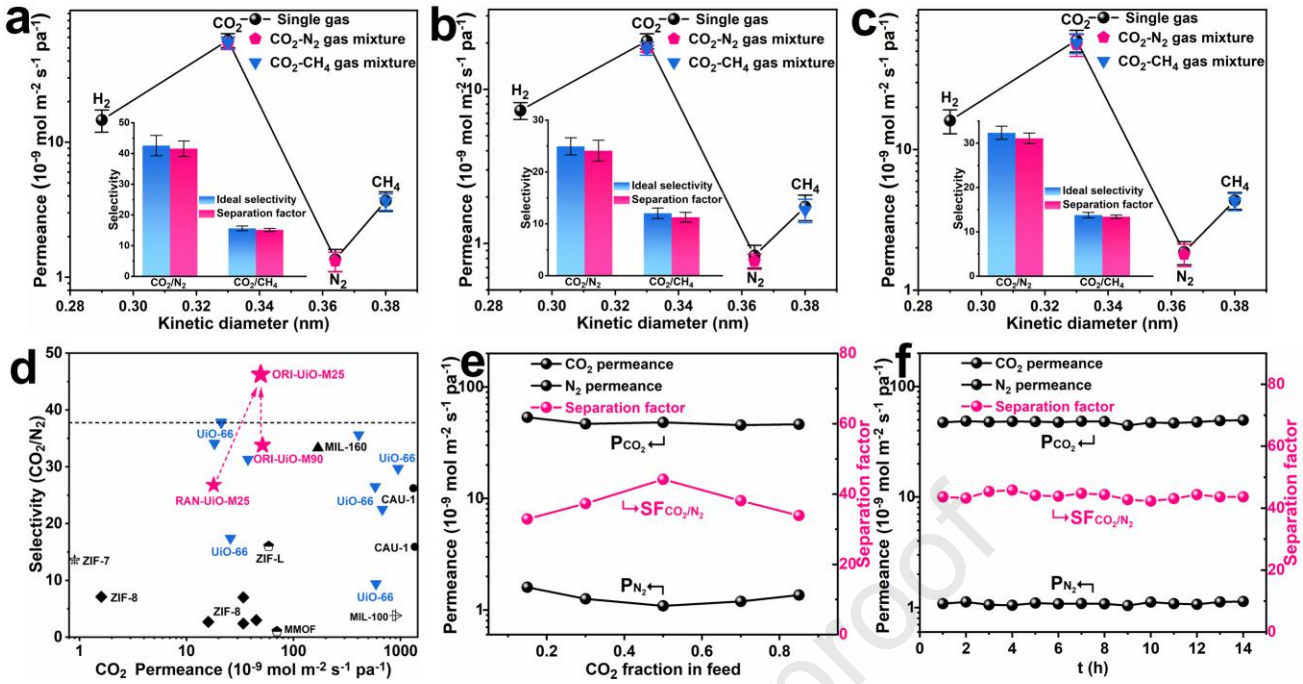

Fig. 5. Results of single-gas and mixed-gas permeations on (a) ORI-UiO-M25, (b) RAN-UiO-M25, and (c) ORI-UiO-M90. Inset: SF and ideal selectivity towards the gas pair of CO_2/N_2 and CO_2/CH_4. (d) Comparisons of the CO_2/N_2 separation performances of our UiO-66 membranes with other pure MOF membranes measured in similar conditions. (e) The CO_2/N_2 separation performance as the function of feed compositions of ORI-UiO-M25. (f) Long-term stability test of ORI-UiO-M25 towards equimolar CO_2/N_2 gas pair at 25 °C and 1 bar.

4. Conclusions

In this study, we proposed a multi-scale defect tailoring strategy to rationally design and prepare highly (111)-oriented defect-engineered UiO-66 membrane exhibiting unprecedented CO_2/N_2 selectivity. Among various experimental factors, employing $Zr_6O_4(OH)_4(OAc)_{12}$ clusters as zirconium source and conducting reaction at RT warranted not only the higher missing-linker numbers in UiO-66 frameworks at the microscopic scale but also better maintance of preferred orientations inherited from UiO-66 seed monolayer during epitaxial growth at the mesoscopic scale, which cooperatively contributed to enhanced CO_2/N_2 separation performance. The ideal CO_2/N_2 selectivity of prepared

UiO-66 membrane ranked the highest among all pristine pure MOF membranes measured in similar operating conditions, thus confirming the effectiveness of multi-scale defect tailoring strategy in exceeding performance limits of state-of-the-art MOF membranes. The above strategy was expected to be expanded for facile and mild preparation of diverse state-of-the-art MOF membranes.

CRediT authorship contribution statement

Jiahui Yan: Finished major experiments and relevant characterizations. **Taotao Ji:** Assisted in drawing the schematic illustration and the morphological characterization. **Yanwei Sun:** Helped with the gas permeation test. **Shengyan Meng and Chen Wang:** Helped with the analysis of experimental data. **Yi Liu:** Conceived the idea, projected relevant experiments, and jointly wrote the manuscript with contributions from all authors.

Declaration of competing interest

The authors declare that they have no known competing financial interests or personal relationships that could have appeared to influence the work reported in this paper.

Acknowledgements

The authors are grateful to National Natural Science Foundation of China (22078039, 22108025), Postdoctoral Science Foundation of China (2021TQ0054), National Natural Science Foundation of China (21176231), Fok Ying-Tong Education Foundation of China (171063), Science and Technology Innovation Fund of Dalian (2020JJ26GX026), Science Fund for Creative Research Groups of the National Natural Science Foundation of China (22021005), and the National Key Research and Development Program of China (2019YFE0119200) for the financial support.

References

[1] M.R.A. Hamid, Y. Qian, R. Wei, Z. Li, Y. Pan, Z. Lai, H.K. Jeong, Polycrystalline metal-organic framework (MOF) membranes for molecular separations: Engineering prospects and challenges, J. Membr. Sci. 640 (2021) 119802, https://doi.org/10.1016/j.memsci.2021.119802.

[2] H. Chen, C. Li, L. Liu, B. Meng, N. Yang, J. Sunarso, L. Liu, S. Liu, X. Wang, ZIF-67 membranes supported on porous ZnO hollow fibers for hydrogen separation from gas mixtures, J. Membr. Sci. 653 (2022) 120550, https://doi.org/10.1016/j.memsci.2022.120550.

[3] B. Li, X. You, H. Wu, R. Li, K. Xiao, Y. Ren, H. Wang, S. Song, Y. Wang, Y. Pu, X. Huang, Z. Jiang, A facile metal ion pre-anchored strategy for fabrication of defect-free MOF membranes on polymeric substrates, J. Membr. Sci. 650 (2022) 120419, https://doi.org/10.1016/j.memsci.2022.120419.

[4] Q. Ma, X. Wang, H. Jin, S. Feng, W. Fang, Y. Li, Highly permeable ZIF-8 membranes for propylene permselective pervaporation under high pressure up to 20 bar, J. Membr. Sci. 643 (2022) 120055, https://doi.org/10.1016/j.memsci.2021.120055.

[5] Y. Zhao, M. Wu, Y. Guo, N. Mamrol, X. Yang, C. Gao, B. Van Der Bruggen, Metal-organic framework based membranes for selective separation of target ions, J. Membr. Sci. 634 (2021) 119407, https://doi.org/10.1016/j.memsci.2021.119407.

[6] S. Dai, F. Nouar, S. Zhang, A. Tissot, C. Serre, One-step room-temperature synthesis of metal (IV) carboxylate metal-organic frameworks, Angew. Chem. Int. Ed. 60 (2021) 4282-4288, https://doi.org/10.1002/anie.202014184.

[7] X. Wang, Q. Lyu, T. Tong, K. Sun, L.C. Lin, C.Y. Tang, F. Yang, M.D. Guiver, X. Quan, Y. Dong, Robust ultrathin nanoporous MOF membrane with intra-crystalline defects for fast water transport, Nat. Commun. 13 (2022) 266, https://doi.org/10.1038/s41467-021-27873-6.

[8] Y. Sun, Y. Liu, J. Caro, X. Guo, C. Song, Y. Liu, In-plane epitaxial growth of highly c-oriented NH_2-MIL-125(Ti) membranes with superior H_2/CO_2 selectivity, Angew. Chem. Int. Ed. 57 (2018) 16088-16093, https://doi.org/10.1002/anie.201810088.

[9] Y. Song, Y. Sun, D. Du, M. Zhang, Y. Liu, L. Liu, T. Ji, G. He, Y. Liu, Fabrication of c-oriented ultrathin TCPP-derived 2D MOF membrane for precise molecular sieving, J. Membr. Sci. 634 (2021) 119393, https://doi.org/10.1016/j.memsci.2021.119393.

[10] B. Ghalei, K. Wakimoto, C.Y. Wu, A.P. Isfahani, T. Yamamoto, K. Sakurai, M. Higuchi, B.K. Chang, S. Kitagawa, E. Sivaniah, Rational tuning of zirconium metal-organic framework membranes for hydrogen purification, Angew. Chem. Int. Ed. 58 (2019) 19034-19040, https://doi.org/10.1002/anie.201911359.

[11] M. Shah, M.C. McCarthy, S. Sachdeva, A.K. Lee, H.K. Jeong, Current status of metal-organic framework membranes for gas separations: Promises and challenges, Ind. Eng. Chem. Res. 51 (2012) 2179-2199, https://doi.org/10.1021/ie202038m.

[12] Y. Mao, L. Shi, H. Huang, W. Cao, J. Li, L. Sun, X. Jin, X. Peng, Room temperature synthesis of free-standing HKUST-1 membranes from copper hydroxide nanostrands for gas separation, Chem. Commun. 49 (2013) 5666-5668, https://doi.org/10.1039/c3cc42601g.

[13] Y. Pan, Z. Lai, Sharp separation of C2/C3 hydrocarbon mixtures by zeolitic imidazolate framework-8 (ZIF-8) membranes synthesized in aqueous solutions, Chem. Commun. 47 (2011) 10275-10277, https://doi.org/10.1039/c1cc14051e.

[14] J. Hou, P.D. Sutrisna, Y. Zhang, V. Chen, Formation of ultrathin, continuous metal-organic framework membranes on flexible polymer substrates, Angew. Chem. Int. Ed. 55 (2016) 3947-3951, https://doi.org/10.1002/anie.201511340.

[15] J.H. Cavka, S. Jakobsen, U. Olsbye, N. Guillou, C. Lamberti, S. Bordiga, K.P. Lillerud, A new zirconium inorganic building brick forming metal organic frameworks with exceptional stability, J. Am. Chem. Soc. 130 (2008) 13850-13851, https://doi.org/10.1021/ja8057953.

[16] X. Liu, Metal-organic framework UiO-66 membranes, Front. Chem. Sci. Eng. 14 (2020) 216-232, https://doi.org/10.1007/s11705-019-1857-5.

[17] F. Wu, L. Lin, H. Liu, H. Wang, J. Qiu, X. Zhang, Synthesis of stable UiO-66 membranes for pervaporation separation of methanol/methyl tert-butyl ether mixtures by secondary growth, J. Membr. Sci. 544 (2017) 342-350, https://doi.org/10.1016/j.memsci.2017.09.047.

[18] X. Liu, C. Wang, B. Wang, K. Li, Novel organic-dehydration membranes prepared from zirconium metal-organic frameworks, Adv. Funct. Mater. 27 (2017) 1604311, https://doi.org/10.1002/adfm.201604311.

[19] F. Wu, Y. Cao, H. Liu, X. Zhang, High-performance UiO-66-NH_2 tubular membranes by zirconia-induced synthesis for desulfurization of model gasoline via pervaporation, J. Membr. Sci. 556 (2018) 54-65, https://doi.org/10.1016/j.memsci.2018.03.090.

[20] J. Yan, Y. Sun, T. Ji, L. Liu, M. Zhang, Y. Liu, Cooperative defect tailoring: A promising protocol for exceeding performance limits of state-of-the-art MOF membranes, J. Membr. Sci. 635 (2021) 119515, https://doi.org/10.1016/j.memsci.2021.119515.

[21] X. Liu, N.K. Demir, Z. Wu, K. Li, Highly water-stable zirconium metal organic framework UiO-66 membranes supported on alumina hollow fibers for desalination, J. Am. Chem. Soc. 137 (2015) 6999-7002, https://doi.org/10.1021/jacs.5b02276.

[22] R. Rong, Y. Sun, T. Ji, Y. Liu, Fabrication of highly CO_2/N_2 selective polycrystalline UiO-66 membrane with two-dimensional transition metal dichalcogenides as zirconium source via solvothermal, J. Membr. Sci. 610 (2020) 118275, https://doi.org/10.1016/j.memsci.2020.118275.

[23] Y. Sun, C. Song, X. Guo, Y. Liu, Concurrent manipulation of out-of-plane and regional in-plane orientations of NH_2-UiO-66 membranes with significantly reduced anisotropic grain boundary and superior H_2/CO_2 separation performance, ACS Appl. Mater. Interfaces 12 (2020) 4494-4500, https://doi.org/10.1021/acsami.9b18804.

[24] W. Wu, Z. Li, Y. Chen, W. Li, Polydopamine-modified metal-organic framework membrane with enhanced selectivity for carbon capture, Environ. Sci. Technol. 53 (2019) 3764-3772, https://doi.org/10.1021/acs.est.9b00408.

[25] G. Yu, X. Zou, L. Sun, B. Liu, Z. Wang, P. Zhang, G. Zhu, Constructing connected paths between UiO-66 and PIM-1 to improve membrane CO_2 separation with crystal-like gas selectivity, Adv. Mater. 31 (2019) 1806853, https://doi.org/10.1002/adma.201806853.

[26] S. Friebe, B. Geppert, F. Steinbach, J. Caro, Metal-organic framework UiO-66 layer: A highly oriented membrane with good selectivity and hydrogen permeance, ACS Appl. Mater. Interfaces 9 (2017) 12878-12885, https://doi.org/10.1021/acsami.7b02105.

[27] V. Guillerm, S. Gross, C. Serre, T. Devic, M. Bauer, G. Ferey, A zirconium methacrylate oxocluster as precursor for the low-temperature synthesis of porous zirconium(IV) dicarboxylates, Chem. Commun. 46 (2010) 767-769, https://doi.org/10.1039/b914919h.

[28] M.R. DeStefano, T. Islamoglu, J.T. Hupp, O.K. Farha, Room-temperature synthesis of UiO-66 and thermal modulation of densities of defect sites, Chem. Mater. 29 (2017) 1357-1361, https://doi.org/10.1021/acs.chemmater.6b05115.

[29] T.H. Lee, A. Ozcan, I. Park, D. Fan, J.K. Jang, P.G.M. Mileo, S.Y. Yoo, J.S. Roh, J.H. Kang, B.K. Lee, Y.H. Cho, R. Semino, H.W. Kim, G. Maurin, H.B. Park, Disclosing the role of defect-engineered metal-organic frameworks in mixed matrix membranes for efficient CO_2 separation: A joint experimental-computational exploration, Adv. Funct. Mater. 31 (2021) 2103973, https://doi.org/10.1002/adfm.202103973.

[30] H. Wu, Y.S. Chua, V. Krungleviciute, M. Tyagi, P. Chen, T. Yildirim, W. Zhou, Unusual and highly tunable missing-linker defects in zirconium metal-organic framework UiO-66 and their important effects on gas adsorption, J. Am. Chem. Soc. 135 (2013) 10525-10532, https://doi.org/10.1021/ja404514r.

[31] Y. Feng, Q. Chen, M. Jiang, J. Yao, Tailoring the properties of UiO-66 through defect engineering: A review, Ind. Eng. Chem. Res. 58 (2019) 17646-17659, https://doi.org/10.1021/acs.iecr.9b03188.

[32] S. Dissegna, K. Epp, W.R. Heinz, G. Kieslich, R.A. Fischer, Defective metal-organic frameworks, Adv. Mater. 30 (2018) 1704501, https://doi.org/10.1002/adma.201704501.

[33] G.C. Shearer, S. Chavan, S. Bordiga, S. Svelle, U. Olsbye, K.P. Lillerud, Defect engineering: Tuning the porosity and composition of the metal-organic framework UiO-66 via modulated synthesis, Chem. Mater. 28 (2016) 3749-3761, https://doi.org/10.1021/acs.chemmater.6b00602.

[34] L. Liu, Z. Chen, J. Wang, D. Zhang, Y. Zhu, S. Ling, K.W. Huang, Y. Belmabkhout, K. Adil, Y. Zhang, B. Slater, M. Eddaoudi, Y. Han, Imaging defects and their evolution in a metal-organic framework at sub-unit-cell resolution, Nat. Chem. 11 (2019) 622-628, https://doi.org/10.1038/s41557-019-0263-4.

[35] Z. Fang, B. Bueken, D.E. De Vos, R.A. Fischer, Defect-engineered metal-organic frameworks, Angew. Chem. Int. Ed. 54 (2015) 7234-7254, https://doi.org/10.1002/anie.201411540.

[36] C. Zhang, J. Yan, T. Ji, D. Du, Y. Sun, L. Liu, X. Zhang, Y. Liu, Fabrication of highly (110)-Oriented ZIF-8 membrane at low temperature using nanosheet seed layer, J. Membr. Sci. 641 (2022) 119915, https://doi.org/10.1016/j.memsci.2021.119915.

[37] Y. Sun, D. Yan, Y. Wu, F.Y. Shih, C. Zhang, H. Luo, S.H. Lin, Y. Liu, Fabrication of twin-free ultrathin NH_2-MIL-125(Ti) membrane with c-preferred orientation using transition-metal trichalcogenides as titanium source, ACS Mater. Lett. 4 (2022) 55-60, https://doi.org/10.1021/acsmaterialslett.1c00452.

[38] Y. Li, H. Liu, H. Wang, J. Qiu, X. Zhang, GO-guided direct growth of highly oriented metal organic framework nanosheet membranes for H_2/CO_2 separation, Chem. Sci. 9 (2018) 4132-4141, https://doi.org/10.1039/c7sc04815g.

[39] B. Shan, J.B. James, M.R. Armstrong, E.C. Close, P.A. Letham, K. Nikkhah, Y.S. Lin, B. Mu, Influences of deprotonation and modulation on nucleation and growth of UiO-66: Intergrowth and orientation, J. Phys. Chem. C 122 (2018) 2200-2206, https://doi.org/10.1021/acs.jpcc.7b11012.

[40] D.C. Oliveira, A.G. Macedo, N.J.O. Silva, C. Molina, R.A.S. Ferreira, P.S. Andre, K. Dahmouche, V.D.Z. Bermudez, Y. Messaddeq, S.J.L. Ribeiro, L.D. Carlos, Photopatternable di-ureasil-zirconium oxocluster organic-inorganic hybrids as cost effective integrated optical substrates, Chem. Mater. 20 (2008) 3696-3705, https://doi.org/10.1021/cm7031702.

[41] J. Yan, Y. Sun, T. Ji, C. Zhang, L. Liu, Y. Liu, Room-temperature synthesis of defect-engineered Zirconium-MOF membrane enabling superior CO_2/N_2 selectivity with zirconium-oxo cluster source, J. Membr. Sci. 653 (2022) 120496, https://doi.org/10.1016/j.memsci.2022.120496.

[42] T.H. Lee, J.G. Jung, Y.J. Kim, J.S. Roh, H.W. Yoon, B.S. Ghanem, H.W. Kim, Y.H. Cho, I. Pinnau, H.B. Park, Defect engineering in metal-organic frameworks towards advanced mixed matrix membranes for efficient propylene/propane separation, Angew. Chem. Int. Ed. 60 (2021) 13081-13088, https://doi.org/10.1002/anie.202100841.

[43] Y. Zhao, Q. Zhang, Y. Li, R. Zhang, G. Lu, Large-scale synthesis of monodisperse UiO-66 crystals with tunable sizes and missing linker defects via acid/base co-modulation, ACS Appl. Mater. Interfaces 9 (2017) 15079-15085, https://doi.org/10.1021/acsami.7b02887.

[44] H. Bux, A. Feldhoff, J. Cravillon, M. Wiebcke, Y.S. Li, J. Caro, Oriented zeolitic imidazolate framework-8 membrane with sharp H_2/C_3H_8 molecular sieve separation, Chem. Mater. 23 (2011) 2262-2269, https://doi.org/10.1021/cm200555s.

[45] R. Wei, X. Liu, Z. Zhou, C. Chen, Y. Yuan, Z. Li, X. Li, X. Dong, D. Lu, Y. Han, Z. Lai, Carbon nanotube supported oriented metal organic framework membrane for effective ethylene/ethane separation, Sci. Adv. 8 (2022) eabm6741, https://doi.org/10.1126/sciadv.abm6741.

[46] D. Yang, S.O. Odoh, J. Borycz, T.C. Wang, O.K. Farha, J.T. Hupp, C.J. Cramer, L. Gagliardi, B.C. Gates, Tuning Zr-6 metal-organic framework (MOF) nodes as catalyst supports: Site densities and electron-donor properties influence molecular iridium complexes as ethylene conversion catalysts, ACS Catal. 6 (2016) 235-247, https://doi.org/10.1021/acscatal.5b02243.

[47] D. Yang, S.O. Odoh, T.C. Wang, O.K. Farha, J.T. Hupp, C.J. Cramer, L. Gagliardi, B.C. Gates, Metal-organic framework nodes as nearly ideal supports for molecular catalysts: NU-1000-and UiO-66-supported iridium complexes, J. Am. Chem. Soc. 137 (2015) 7391-7396, https://doi.org/10.1021/jacs.5b02956.

[48] K. Chen, K. Xu, L. Xiang, X. Dong, Y. Han, C. Wang, L.B. Sun, Y. Pan, Enhanced CO_2/CH_4 separation performance of mixed-matrix membranes through dispersion of sorption-selective MOF nanocrystals, J. Membr. Sci. 563 (2018) 360-370, https://doi.org/10.1016/j.memsci.2018.06.007.

[49] W. Liang, C.J. Coghlan, F. Ragon, M. Rubio-Martinez, D.M. D'Alessandro, R. Babarao, Defect engineering of UiO-66 for CO_2 and H_2O uptake - a combined experimental and simulation study, Dalton Trans. 45 (2016) 4496-4500, https://doi.org/10.1039/c6dt00189k.

[50] C. Chmelik, H. Bux, H. Voss, J. Caro, Adsorption and diffusion - basis for molecular understanding of permeation through molecular sieve membranes, Chem. Ing. Tech. 83 (2011) 104-112, https://doi.org/10.1002/cite.201000179.

[51] W.J. Koros, C. Zhang, Materials for next-generation molecularly selective synthetic membranes, Nat. Mater. 16 (2017) 289-297, https://doi.org/10.1038/nmat4805.

- CO_2/N_2 separation performance of (111)-oriented UiO-66 membrane exceeded the upper limits of pristine MOF membranes
- Conducting reaction at room temperature with $Zr_6O_4(OH)_4(OAc)_{12}$ cluster source warranted better preferred orientation control
- This represented the first room-temperature preparation of oriented high-valent transition metal-oxo node-based MOF membranes

Author Statement

Jiahui Yan: Completed the main experiments and relevant characterizations, co-wrote the manuscript with contributions from all authors. **Taotao Ji:** Assisted in synthesizing UiO-66 membranes. **Yanwei Sun:** Helped with the analysis of experimental data. **Shengyan Meng:** Assisted in characterization and analysis of Liquid ^{1}H NMR. **Chen Wang:** Assisted in related morphological characterization. **Yi Liu:** Conceived the idea and designed the experiments, co-wrote the manuscript with contributions from all authors.

Declaration of interests

☒ The authors declare that they have no known competing financial interests or personal relationships that could have appeared to influence the work reported in this paper.

☐The authors declare the following financial interests/personal relationships which may be considered as potential competing interests: